International Journal of Heat and Technology
Vol. 44, No. 2, April, 2026, pp. 645-659
Journal homepage: http://iieta.org/journals/ijht

Multiphase Computational Fluid Dynamics Analysis of Hydro-Abrasive Wear in Slurry Pipelines Using the Oka Erosion Model with Ultrasonic Validation

Diana Beltrán Quispe*, Paul Otazú Ayque, Luis Lazo Alarcon, Viviana Beltrán Quispe

Department of Materials Engineering, Universidad Nacional de San Agustín de Arequipa, Arequipa 04000, Peru

Corresponding Author Email: dbeltranq@unsa.edu.pe

https://doi.org/10.18280/ijht.440218

Received: 16 January 2026
Revised: 8 April 2026
Accepted: 17 April 2026
Available online: 30 April 2026

Keywords:
Alumina ceramics, Computational Fluid Dynamics, copper slurry, erosion modeling, hydro-abrasive wear, multiphase flow, Oka theory, ultrasonic validation

ABSTRACT

This study investigates hydro-abrasive wear mechanisms in cyclone feed slurry pipelines used in copper processing plants, focusing on localized failure at Y junction interfaces where empirical criteria are insufficient. A high-fidelity Eulerian-Lagrangian Computational Fluid Dynamics coupled with the Discrete Phase Model (CFD-DPM) framework was implemented, incorporating the Herschel Bulkley model to represent non-Newtonian slurry behavior and Oka's erosion formulation to describe particle wall interactions. Model predictions were assessed against Ultrasonic Testing (UT) data obtained from Spool 32 using a SIUI SMARTOR device, yielding a Normalized Root Mean Square Error (NRMSE) of 6.8%. Due to the limitations of UT for composite linings, this comparison represents an indirect validation of the predicted wear patterns. Results indicate that asymmetric momentum redistribution and high velocity impingement generate localized degradation, with a minimum residual thickness of 10.7 mm identified in critical zones. Erosion scaling analysis shows that material response is governed by hardness dependent regimes, placing elastomeric and ceramic linings in distinct erosion domains under equivalent operating conditions. These findings support the use of alumina based linings in high impact regions and provide a physically grounded framework for material selection and maintenance planning in slurry transport systems.

1. INTRODUCTION

In the contemporary context of global copper production, the efficiency of comminution and classification circuits is a primary determinant of operational throughput [1, 2]. As ore grades decline, mineral processing plants are required to increase volumetric flow rates, placing greater demands on hydraulic transport systems. Within these circuits, the transport of cyclone feed slurry, a mixture of crushed ore and water, represents one of the most abrasive and energy intensive stages [3, 4]. Therefore, the structural integrity of pipelines connecting Semi-Autogenous Grinding (SAG) mills to cyclone clusters is critical [5], as any unplanned interruption directly halts the concentration process and leads to significant economic losses [6, 7].

During operation, ground ore discharged from the SAG mill is classified using vibratory screens [8]. The undersized fraction is collected in a sump, mixed with process water, and pumped toward the cyclone system [9, 10]. However, due to the stochastic nature of screening, oversized particles (up to 30 mm) may bypass classification. When transported under high-velocity conditions, these coarse particles exhibit inertial decoupling, where their kinetic energy exceeds the viscous resistance of the carrier fluid, generating severe particle-wall impacts.

Hydro-abrasive erosion in slurry pipelines is inherently non-uniform. In complex geometries such as Y-junctions and bypass branches, the flow is subjected to strong pressure gradients and secondary structures, including Dean vortices [11, 12]. These effects lead to localized impact concentration and the formation of severe wear hotspots that cannot be accurately predicted using conventional empirical correlations. A representative case is observed in Emergency Spool 31, where flow fluctuations create a stagnant region that promotes the accumulation of fine and coarse particles [13, 14]. This sedimentation alters local flow behavior and requires mechanical removal prior to inspection procedures such as Ultrasonic Testing (UT).

Field observations indicate a pronounced circumferential asymmetry in wear patterns, with accelerated degradation in lower regions due to gravitational settling. In addition, interactions between oversized particles and multi-material linings result in localized spalling and abrasive mechanisms, often requiring temporary mitigation strategies such as sacrificial coatings [15, 16]. Despite these operational challenges, there remains a lack of high-fidelity numerical approaches capable of capturing both variable pumping conditions and large-particle erosion mechanisms in industrial-scale systems [17, 18]. Recent studies in coupled multiphysics systems have highlighted the importance of integrated numerical frameworks for resolving complex engineering interactions [19, 20].

The spatial configuration of the grinding-classification circuit plays a critical role in defining hydrodynamic behavior

and wear intensity [21]. As illustrated in Figure 1, the system operates as a closed loop in which the cyclone feed sump acts as the primary convergence node. At this stage, SAG mill discharge is combined with recirculated material from the ball mill, forming a complex slurry mixture [22]. This mixture is transported through a sequence of discharge spools driven by high-capacity centrifugal pumps, generating a continuous recirculation of coarse particles. These particles repeatedly traverse the system, intensifying cumulative erosion effects, particularly at geometrical transitions such as Spool 31.

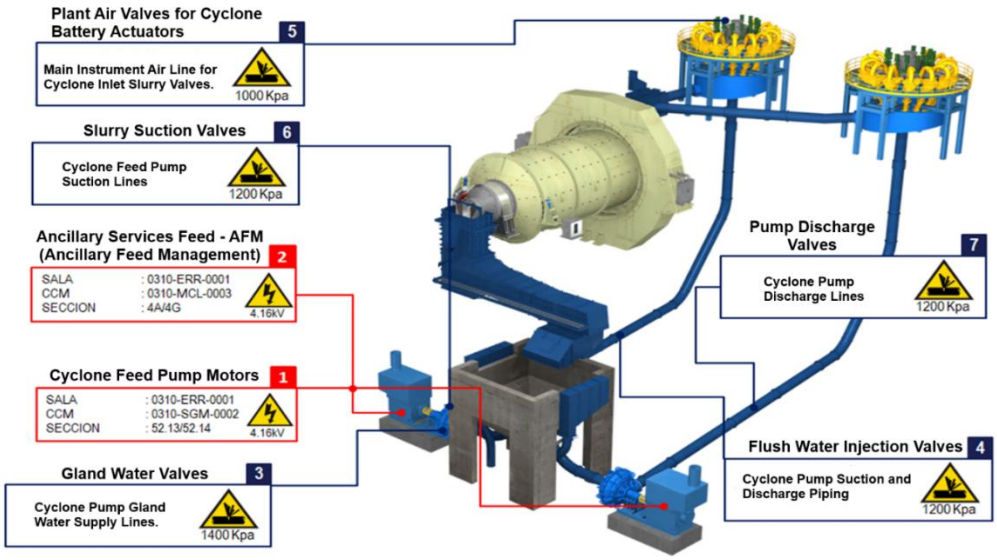

Figure 1. Closed-circuit grinding layout: Ball mill regrinding path and cyclone classification loop

To address these limitations, this study develops a high-fidelity computational framework based on Eulerian-Lagrangian Computational Fluid Dynamics coupled with the Discrete Phase Model (CFD-DPM) combined with Oka's erosion model to resolve fluid–particle interactions at the wall interface. The objective is to quantify the influence of inertial decoupling on erosion patterns in multi-material linings, specifically natural rubber and alumina ceramics, and to evaluate the predictive capability of the model through comparison with in-situ ultrasonic measurements. Additionally, this work aims to establish a methodology for estimating the Remaining Useful Life (RUL) of critical pipeline components under realistic operating conditions, providing a physically grounded basis for optimizing material selection and maintenance strategies in slurry transport systems.

2. SYSTEM CHARACTERIZATION AND EXPERIMENTAL BASELINE

2.1 From blueprints to Computer-Aided Design: Geometric reconstruction of spool 31

The geometric fidelity of the computational domain is a fundamental requirement for reliable Computational Fluid Dynamics (CFD) predictions [23, 24]. In this study, the discharge assembly, comprising the suction line, the Warman 650 MCR-M200 pump, and the sequence of spools from 26 to 38, was reconstructed from original manufacturer blueprints. The resulting three-dimensional Computer-Aided Design (CAD) model, developed at full scale in SolidWorks, captures the internal flow passages and the bifurcation associated with the emergency discharge system, as shown in Figure 2.

This geometric reconstruction enables the identification of localized features that govern hydrodynamic behavior and wear distribution. In particular, Spool 31 exhibits a Y-junction configuration in which the main branch ascends at 45° toward the cyclone cluster, while the secondary horizontal branch functions as an emergency discharge and maintenance outlet. Under normal operating conditions, this lateral branch remains closed, forming a low-velocity region where particulate matter accumulates. This accumulation modifies the local flow structure and must be removed prior to inspection procedures such as UT.

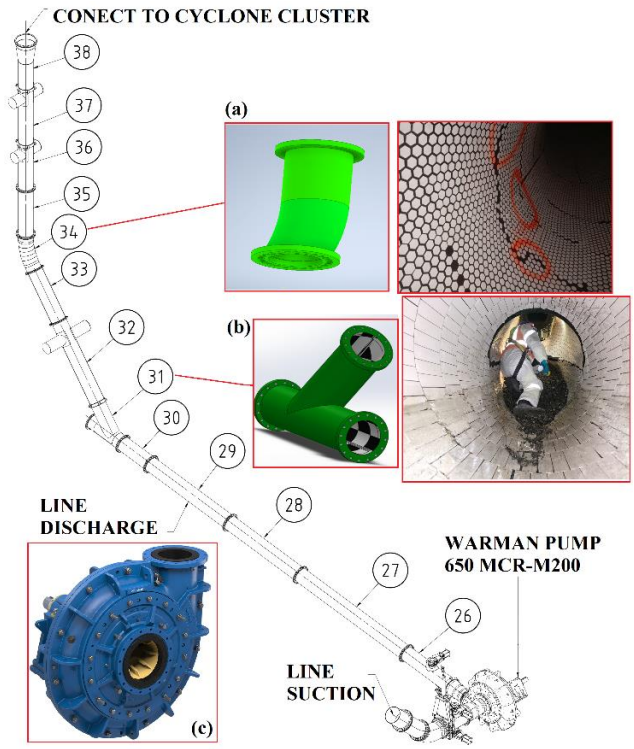

Figure 2. Isometric Computer-Aided Design (CAD) of discharge system: (a) Pump assembly, (b) Spool 31 rectangular lining, and (c) Spool 34 hexagonal lining

Due to its critical location within the system, Spool 31 incorporates an increased lining thickness. The internal protection is based on rectangular ceramic tiles arranged to minimize interfacial discontinuities and reduce localized erosion at joints. In contrast, Spool 34, an elbow responsible for redirecting the flow toward a vertical trajectory, employs a hexagonal ceramic configuration, which provides improved surface conformity in curved regions and enhances coverage continuity.

The reconstructed geometry explicitly includes the nominal thickness of the multi-material lining system. This ensures that the computational domain accurately represents the effective internal diameter and the fluid–structure interface, allowing for consistent evaluation of flow patterns and erosion mechanisms under representative operating conditions.

2.2 Variable pumping dynamics: Warman pump cycles and flow analysis

The hydraulic behavior of the classification circuit is governed by the performance of the centrifugal pumping system. The Warman 650 MCR-M200 pump, shown in Figure 3, operates with an 8° tangential discharge configuration, while the suction system integrates the manifold corresponding to Spools 21–24.

To establish physically consistent boundary conditions, the relationship between impeller rotational speed N and volumetric flow rate Q was defined using the pump affinity laws, following Visintainer et al. [25]. These relationships can be expressed as:

$$\frac{Q_1}{Q_2} = \frac{N_1}{N_2} \; ; \; \frac{H_1}{H_2} = \left(\frac{N_1}{N_2}\right)^2 \; ; \; \frac{P_1}{P_2} = \left(\frac{N_1}{N_2}\right)^3 \tag{1}$$

Operational data obtained from the Variable Frequency Drive (VFD) system over a six-month period were analyzed to characterize flow variability. The recorded signals showed fluctuations in rotational speed within a defined operating window, which were incorporated into the numerical model as discrete steady-state conditions representative of low, nominal, and high flow regimes. This approach provides a practical approximation of transient behavior while maintaining computational tractability.

Under reduced flow conditions, the capacity of the carrier fluid to maintain coarse particles in suspension decreases significantly. This effect was evaluated using the Archimedes number, defined as [25]:

$$Ar = \frac{g d_p^3 \rho(\rho_p - \rho)}{\mu^2} \tag{2}$$

where, g is gravitational acceleration, d_p is the particle diameter (up to 30 mm for oversized fragments), ρ_s and ρ_f are the solid and fluid densities, and μ is the dynamic viscosity of the slurry. The resulting Archimedes number indicates that gravitational forces dominate over viscous effects during low-velocity regimes, promoting particle settling in regions with reduced flow momentum, particularly within the lateral branch of Spool 31.

The set of components included in the geometric reconstruction is summarized in Table 1, where Spool 31 (Y-junction) is defined as the primary computational domain. This location represents a critical transition zone where the initial 8° discharge inclination evolves into a 45° ascending flow toward the cyclone system, generating complex hydrodynamic conditions that directly influence erosion patterns.

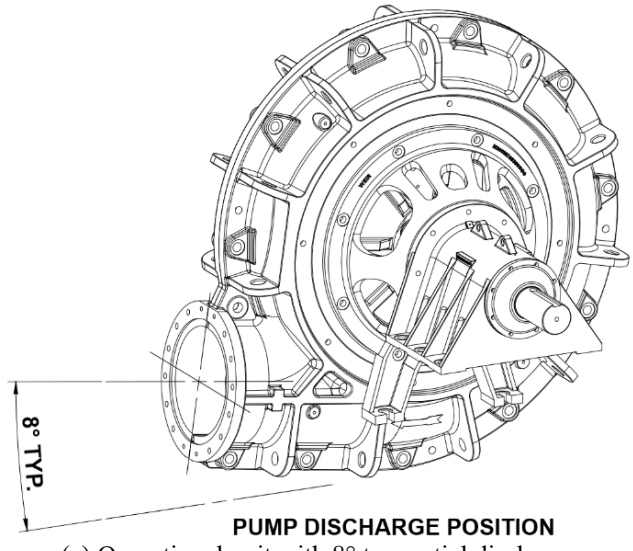

(a) Operational unit with 8° tangential discharge

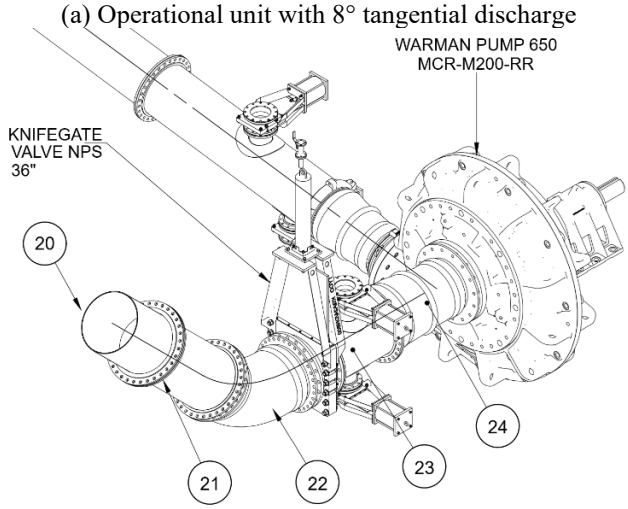

(b) Isometric view of the suction manifold (Spools 21–24)

Figure 3. Warman 650 MCR-M200 pump configuration

Table 1. Technical specifications of the suction and discharge line components

Component ID	Description
20	Sacrifice Spool NPS 36"
21	Spool NPS 36"
22	Preformado Elbow
23	Spool NPS 36"
24	Rubber Join External I.D. 34° × I.D. 30"
25	Rubber Join External I.D. 710 × I.D. 660
26	Spool NPS 32" × 12" × 2"
27	Spool NPS 32" × 7658 L.
28	Spool NPS 32" × 6027 L.
29	Spool NPS 32" × 6027 L.
30	Spool NPS 32" × 2100 L.
31	Spool Y-junction NPS 32" × 45° (Primary Computational Domain)
32	Spool NPS 32" × 4964 L.
33	Spool NPS 32" × 3027 L.
34	Spool Bend NPS 32" × 37° × 3D
35	Spool NPS 32" × 3027 L.
36	Spool NPS 32" × 2911 L.
37	Spool NPS 32" × 3949 L.
38	Spool Reduc. Conc. NPS 42" × 32" × 4033 L.

Note: Nominal Pipe Size (NPS); Internal Diameter (I.D.).

2.3 Multi-material lining systems: Tribological properties

The internal protection system implemented in Spool 31 is based on a hybrid lining architecture designed to mitigate multiple wear mechanisms associated with hydro-abrasive flow. This configuration combines high-purity alumina (Al_2O_3) ceramic tiles, which provide resistance to sliding abrasion, with a natural rubber backing layer that enhances impact energy dissipation from coarse particles.

To assess the integrity of the ceramic–elastomer interface, a qualitative microstructural analysis was conducted using Scanning Electron Microscopy (SEM) [26, 27]. The objective of this characterization was to verify the continuity of the bonding interface and to identify potential discontinuities that could act as stress concentrators under cyclic loading conditions.

Figure 4 shows a representative SEM micrograph of the alumina–rubber interface. The ceramic phase exhibits a dense polycrystalline structure with well-defined grain boundaries and no evidence of interfacial debonding or porosity. The absence of microcracks or voids indicates effective mechanical coupling between the ceramic tiles and the elastomeric substrate. This interfacial continuity is essential to reduce stress localization and delay the onset of ceramic spalling under repeated particle impacts (d_p = 30 mm).

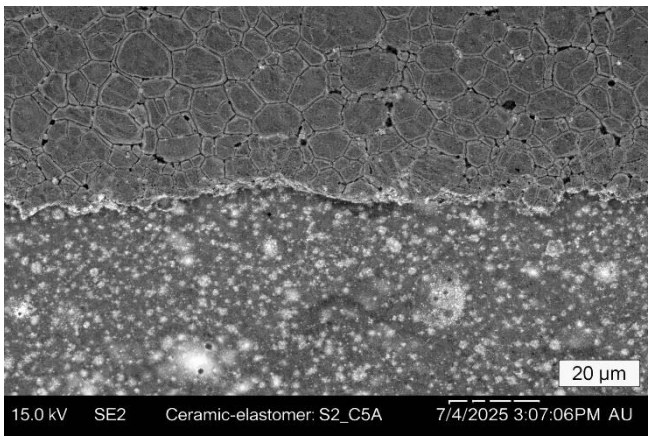

Figure 4. Representative Scanning Electron Microscopy (SEM) micrograph of the alumina–rubber lining interface used in Spool 31

Note: It illustrates the dense ceramic microstructure and the continuous bonding region with the elastomeric substrate

Table 2. Mechanical and tribological properties of the system components

Material Component	Density (ρ) (kg/m^3)	Vickers Hardness (H_v)	Elastic Modulus (E) [GPa]	Poisson Ratio (v)
Natural Rubber Liner	1,150	0.02 – 0.05	0.01 – 0.05	0.49
Alumina Ceramic (Al_2O_3)	3,650	1,100 – 1,550	300 – 380	0.22
Ore Particles (Solid Phase)	2,750 – 3,100	600 - 800	70 – 90	0.25 – 0.30

These observations are consistent with established tribological criteria, where dense ceramic phases combined with compliant substrates improve impact resistance by promoting load redistribution and energy absorption rather than brittle fracture [28, 29].

The mechanical and tribological properties of the system components are summarized in Table 2. These properties, particularly density, hardness, and elastic modulus, constitute key inputs for the erosion model, as they influence particle wall interaction mechanics and energy transfer during impact events.

2.4 In-situ thickness monitoring: Ultrasonic Testing

An experimental monitoring campaign was conducted during scheduled maintenance shutdowns to provide a reference dataset for model validation. Although Spool 31 represents the primary hydrodynamic region of interest, its composite ceramic–rubber lining presents high acoustic impedance, which limits the applicability of conventional ultrasonic pulse-echo techniques for internal thickness measurements.

As a result, direct ultrasonic measurements were not feasible for Spool 31. Instead, inspection of this component was based on visual assessment and localized repair interventions. To establish a quantitative validation baseline, UT was performed on Spool 32, a steel-lined component located immediately downstream, where reliable acoustic measurements can be obtained.

Measurements were acquired using a SIUI SMARTOR ultrasonic gauge equipped with a 1 MHz transducer, calibrated for an acoustic velocity of 1587 m/s and a gain of 38.5 dB. The inspection grid consisted of 12 measurement points distributed across three axial stations: upstream (S1), mid-section (S2), and downstream (S3). At each station, four circumferential positions were evaluated (0°, 90°, 180°, and 270°), as illustrated in Figure 5.

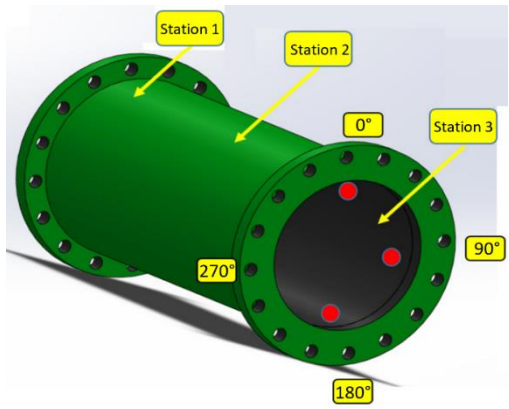

Figure 5. Monitoring grid and spatial discretization of spool 32

The results, summarized in Table 3, reveal a clear asymmetry in wear distribution. The minimum thickness was recorded at the S1–90° position (16.27 mm), while visual inspection identified a localized region of complete lining loss near the coupling interface. Direct mechanical measurement in this region indicated a residual wall thickness of 10.7 mm, corresponding to exposure of the base material (see Figure 6).

This experimental dataset provides an indirect validation reference for the numerical model. Specifically, it enables the comparison between predicted erosion hotspots in Spool 31 and the observed wear patterns in Spool 32, which are physically linked through the flow field exiting the Y-junction. While this approach does not constitute direct validation of the

primary computational domain, it offers a consistent basis for assessing the predictive capability of the model under real operating conditions.

Figure 6. Field Inspection and In-Situ Wear Evidence

Table 3. Ultrasonic Testing (UT) thickness measurement data for spool 32 (Baseline)

Station	0° (Top)	90° (Right)	180° (Bottom)	270° (Left)
S1 (Upstream)	19.20	**16.27***	21.60	19.91
S2 (Mid-section)	19.33	22.75	19.78	19.40
S3 (Downstream)	19.14	19.73	20.15	20.25

Note: 10.7 mm residual thickness (base metal) was measured at the S1-90° interface.

To relate numerical erosion predictions to physical material loss, the simulated mass removal rate is converted into a linear erosion rate. Following the formulation proposed by Blazek [30], the erosion rate at each surface element is defined as:

$$R_{erosion} = \frac{\dot{E}_{mass}}{\rho_{wall} \cdot A_{face}} \tag{3}$$

where, $\dot{E}_{mass}$ is the mass loss rate (kg/s), ρ_{wall} is the material density, and A_{face} is the local surface area. This transformation enables direct comparison with measured thickness loss and supports the statistical validation framework presented in Section 4.

3. NUMERICAL FRAMEWORK: THE 4.1 M ELEMENT MODEL

3.1 High-Fidelity discretization: Grid Convergence Index and mesh independence

The reliability of the CFD solution for Spool 31 is governed by the independence of numerical results from spatial discretization. A hybrid meshing strategy was adopted, combining polyhedral elements in the bulk flow region with 15 structured inflation layers at the fluid–structure interface to accurately resolve near-wall gradients [31, 32].

To justify the selection of the 4.08 million element mesh, a Grid Convergence Index (GCI) analysis was performed. Numerical stability was evaluated using Eq. (4):

$$GCI = \frac{F_s|\epsilon|}{r^p - 1} \tag{4}$$

where, $F_s = 1.25$ is the safety factor and ϵ represents the relative discretization error between successive mesh refinements. The evolution of the erosion rate with increasing mesh density demonstrated asymptotic convergence toward mesh-independent conditions, as summarized in Table 4.

To ensure accurate resolution of the viscous sublayer and wall shear stresses, the mesh was refined until the dimensionless wall distance satisfied the criterion $y^+ < 1.1$ in critical wear regions (Eq. (5)):

$$y^+ = \frac{\rho u_\tau y}{\mu} \tag{5}$$

This near-wall treatment enabled the $k-\omega$ SST turbulence model to achieve high fidelity in predicting boundary layer behavior. Spatial convergence was further verified through the coefficient of determination (R^2) (Eq. (6)):

$$R^2 = 1 - \frac{\sum(y_i - \hat{y}_i)^2}{\sum(y_i - \bar{y})^2} \tag{6}$$

The results of the mesh independence study are summarized in Table 4, where the stability of the maximum localized erosion rate (E_{max}) is evident.

Table 4. Mesh independence study results for Maximum Localized Erosion Rate (E_{max})

Mesh Case	No. of Elements (M)	Emax (Oka Model) (kg/(m²·s))	Relative Error ϵ (%)	GCI (%)
Coarse	1.18	2437.82	--	--
Medium	2.44	2894.16	15.77	4.38
Fine (Selected)	**4.08**	**3021.55**	**4.21**	**1.86**
Extra Fine	5.72	3033.48	0.39	0.47

Note: Grid Convergence Index (GCI).

The transition from the Fine to Extra Fine mesh resulted in a negligible variation of 0.39% in E_{max}, confirming mesh independence. Therefore, the 4.08 M element configuration was adopted for all simulations.

3.2 Eulerian-Lagrangian coupling: Discrete Phase Modeling

The slurry flow was modeled as a multiphase system using a pressure-based Eulerian-Lagrangian framework [33, 34]. The carrier phase—representing water and fine particles—was treated as a continuum governed by the continuity (Eq. (7)) and Navier–Stokes equations (Eq. (8)):

$$\nabla \cdot (\rho \mathrm{v}) = 0 \tag{7}$$

$$\frac{\partial}{\partial t}(\rho \mathrm{v}) + \nabla \cdot (\rho \mathrm{vv}) = -\nabla p + \nabla \cdot (\overline{\tau}) + \rho \mathrm{g} + \mathbf{F} \tag{8}$$

To capture the non-Newtonian behavior of the high-density slurry, the Herschel–Bulkley model was *implemented* following Chhabra and Patel [35]. This formulation incorporates yield stress and shear-thinning behavior (Eq. (9)):

$$\tau = \tau_y + K\dot{\gamma}^n \quad (9)$$

To ensure reproducibility of the rheological and boundary condition setup, the key parameters used in the simulations are summarized in Table 5.

Table 5. Boundary conditions and rheological parameters used in Computational Fluid Dynamics (CFD) simulations

Parameter	Symbol	Value	Units
Inlet velocity (nominal)	U_{in}	7.1	m/s
Velocity range (VFD)	U	6.5–9.5	m/s
Outlet pressure	P_{out}	0 (gauge)	Pa
Slurry density	ρ_f	1350–1550	kg/m³
Solid density	ρ_s	2750–3100	kg/m³
Yield stress	τ_0	15–35	Pa
Consistency index	k	8–20	Pa·s^n
Flow behavior index	n	0.45–0.75	–
Apparent viscosity	μ	0.08–0.25	Pa·s

Note: Variable Frequency Drive (VFD).

The parameter ranges reported in Table 5 were defined based on operational data and correlations from studies [35]. Variability in these parameters constitutes a source of uncertainty, particularly affecting erosion rate predictions.

The discrete phase, consisting of coarse particles with diameters of 13 mm and 30 mm, was modeled by tracking individual trajectories in a Lagrangian reference frame. Particle motion and interphase momentum exchange were solved using Eqs. (10)–(13), following the formulation of Kolev [36]:

$$\frac{d\boldsymbol{u}_p}{dt} = F_D(\boldsymbol{u} - \boldsymbol{u}_p) + \frac{\boldsymbol{g}(\rho_p - \rho)}{\rho_p} + \boldsymbol{F}_{other} \quad (10)$$

where, $F_D(\mathrm{u} - \mathrm{u}_p)$ represents the drag force per unit particle mass. The drag coefficient was calculated using the Morsi–Alexander correlation (Eq. (11)), while lift effects were incorporated via the Saffman force (Eq. (12)):

$$F_D = \frac{18\mu}{\rho_p d_p^2}\frac{C_D Re}{24} \quad (11)$$

$$F_L = 1.615\mu d_p^2(\boldsymbol{u} - \boldsymbol{u}_p)\sqrt{\frac{\rho\dot{\gamma}}{\mu}} \quad (12)$$

The coupling regime between phases was evaluated through the Stokes number (Eq. (13)):

$$Stk = \frac{\rho_p d_p^2 v}{18\mu L} \quad (13)$$

The obtained values ($Stk \gg 1$) confirm that coarse particles follow a ballistic regime, where inertia dominates over fluid drag. This behavior explains the deviation of particle trajectories from streamlines and the concentration of impacts at geometric discontinuities such as the Spool 31 Y-junction.

3.3 Erosion kinetics implementation: Oka model adaptation

The erosion behavior of Spool 31 and Spool 32 was modeled using the Oka erosion formulation, implemented according to the tribological framework described by Hutchings and Shipway [37]. This model relates volumetric material loss to particle impact conditions and material properties (Eqs. (14)–(18)).

To ensure transparency and reproducibility, the empirical constants and particle–wall interaction parameters used in the erosion model are summarized in Table 6.

Table 6. Discrete Phase Modeling (DPM) and Oka model parameters

Parameter	Symbol	Value	Units
Particle diameters	d_p	0.013/0.03	m
Restitution coefficient (normal)	e_n	0.6–0.9	–
Restitution coefficient (tangential)	e_t	0.5–0.8	–
Oka constant	K	1.0×10^{-4} $- 5.0 \times 10^{-4}$	–
Oka exponent	n_1	0.8–1.2	–
Oka exponent	n_2	1.5–2.5	–

The volumetric erosion rate is defined as:

$$E(\alpha) = g(\alpha)E_{90} \quad (14)$$

The reference erosion at normal impact (E_{90}) incorporates the material hardness (H_v) (Eq. (15)):

$$E_{90} = K(H_v)^{k_1}(v_p)^{k_2}(d_p)^{k_3} \quad (15)$$

This allows differentiation between alumina ceramic (H_v = 1550), carbon steel (H_v = 210), and elastomeric materials, explaining the variation in erosion resistance observed experimentally.

The angular dependence of erosion is introduced through the impact function $g(\alpha)$, parameterized by n_1 and n_2 (Eq. (16)).

$$g(\alpha) = (sin\,\alpha)^{n_1}[1 + H_v(1 - sin\,\alpha)]^{n_2} \quad (16)$$

Finally, particle rebound behavior is incorporated through the normal and tangential restitution coefficients (Eqs. (17)-(18)):

$$e_n = 1.0 - 0.99\alpha + 0.53\alpha^2 - 0.47\alpha^3 \quad (17)$$

$$e_t = 1.0 - 0.35\alpha + 0.01\alpha^2 + 0.01\alpha^3 \quad (18)$$

The selected parameter ranges for K, n_1, and n_2 were adopted from established literature [37] and were not calibrated against experimental data. This ensures that the model preserves physical consistency while avoiding overfitting to a single case study.

4. RESULTS: THE CONVERGENCE OF PHYSICS AND REALITY

Before proceeding with the detailed characterization of material degradation, it is necessary to establish the spatial and operational reference frame of the analyzed computational domain. The architecture of the slurry transport system is presented in the isometric view of Figure 2, which must be

interpreted in conjunction with Table 1, where the Component ID links each segment, from the Warman pump discharge (Spool 26) to the cyclone cluster admission (Spool 38), to its physical location within the process line.

Under these conditions, the evaluation sections correspond to transverse interfaces between consecutive spools. Therefore, any reference to a junction denotes the exact transition plane where the hydrodynamic variables were extracted from Ansys Fluent.

To ensure clarity in the interpretation of radial gradients and flow asymmetry, the results are presented as paired datasets, where each subsection includes a cross-sectional contour map and its corresponding velocity profile, enabling direct correlation between qualitative flow structures and quantitative distributions.

4.1 Hydrodynamic characterization and wear correlation

The CFD-based hydrodynamic evaluation provides a mechanistic explanation for the wear patterns observed during the field monitoring campaign [38, 39]. The interaction between velocity distribution, pressure fields, and particle dynamics is analyzed across critical sections of the transport system [40, 41].

4.1.1 Boundary condition validation

Boundary conditions were validated at the inlet and outlet sections. A uniform inlet velocity of 7.1 m/s was imposed (Figure 7(a)), corresponding to nominal operation. At the outlet (Spool 38), the flow develops into a non-uniform profile ranging from 7.80 to 8.50 m/s (Figure 7(c)–(d)), reflecting the combined effects of wall friction and non-Newtonian behavior described by the Herschel–Bulkley model (Eq. (9)). This transition confirms that the internal flow evolution is adequately captured.

4.1.2 High-velocity impingement at the Y-junction (Spools 31–32)

The most critical condition occurs at the Y-junction discharge. As shown in Figure 8(c)–(d), velocity peaks reach 9.04 m/s, with the high-velocity core displaced toward the pipe wall, particularly near the 90°.

This asymmetric distribution generates a localized high-momentum impact region, consistent with field observations, where a minimum residual thickness of 10.7 mm was measured at Station 1 (90°). The spatial agreement indicates that erosion is governed by geometry-induced momentum redistribution rather than uniform shear.

4.1.3 Flow redistribution in the verticalization elbow (Spools 33–35)

At the elbow entry (Figure 9(a), velocity peaks up to 9.45 m/s due to centrifugal effects. However, as the flow transitions vertically (Figure 9(c)), the velocity profile becomes more symmetric, indicating momentum redistribution. This explains the reduced erosion severity in these sections compared to the Y-junction.

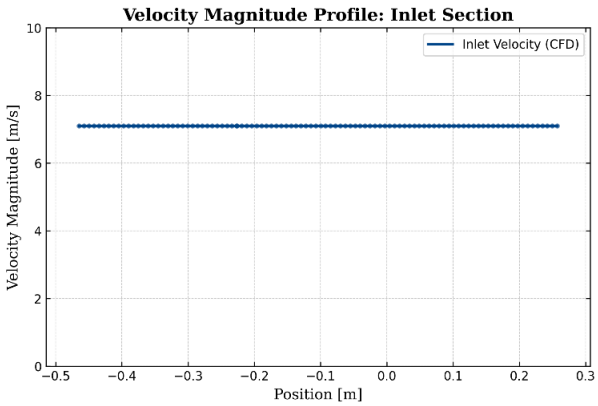

(a) Uniform inlet profile (7.1 m/s)

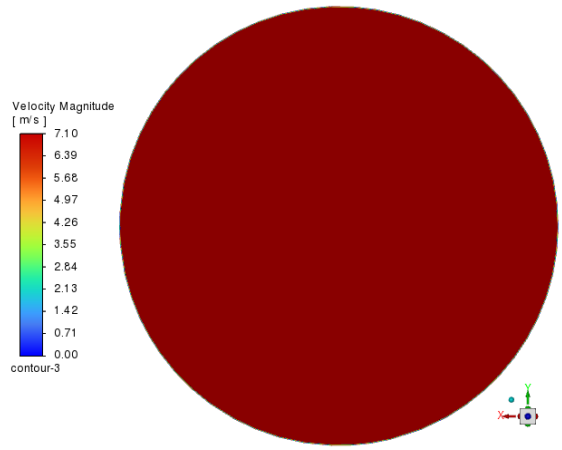

(b) Inlet cross-sectional contour

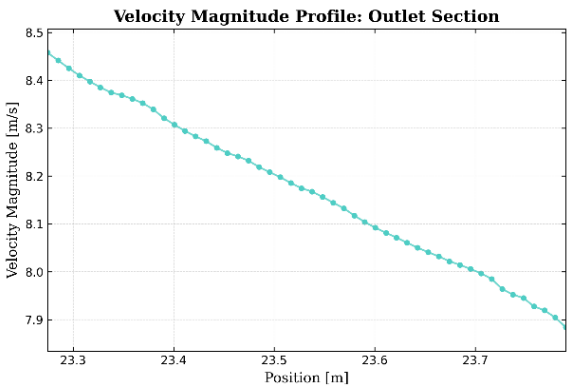

(c) Developed outlet profile

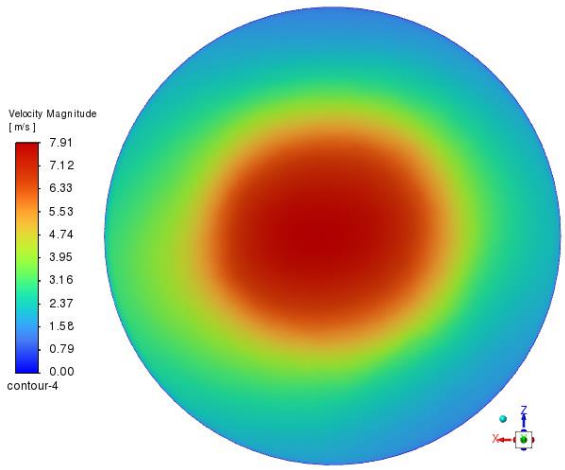

(d) Outlet cross-sectional contour (Spool 38)

Figure 7. Field Velocity magnitude validation at boundary sections

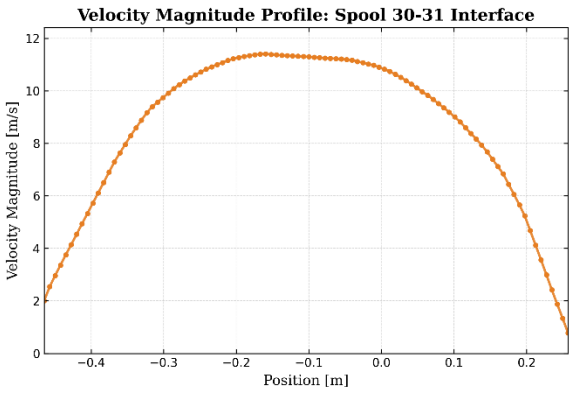

(a) Spool 30–31 velocity profile

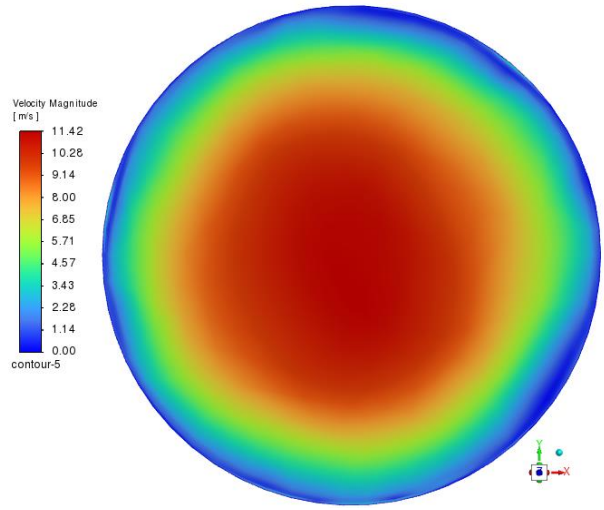

(b) Spool 30-31 cross–sectional contour

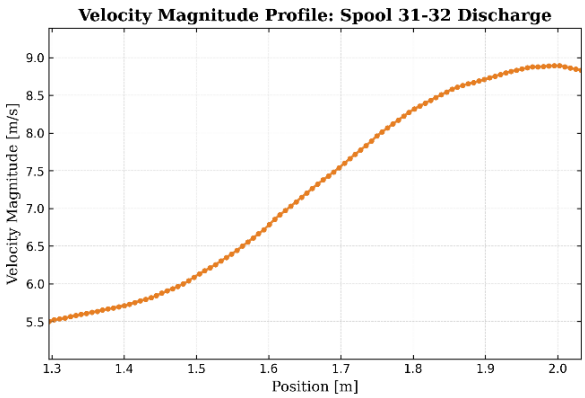

(c) Spool 31–32 discharge profile

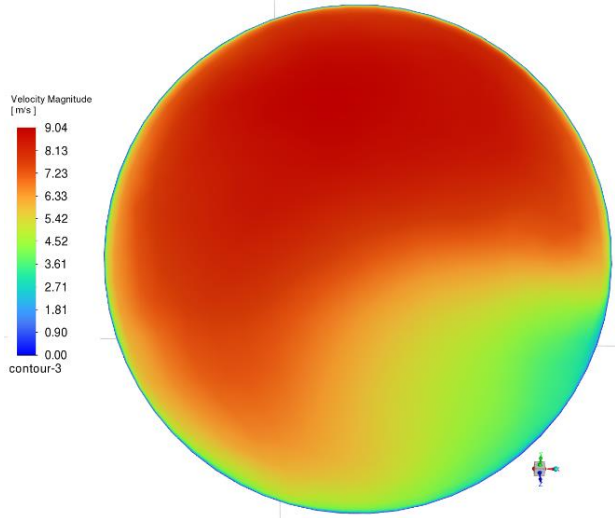

(d) Spool 31–32 cross-sectional contour

Figure 8. Velocity distribution at the Y-junction transition

4.1.4 Localized pressure peaks and mechanical stress

In addition to velocity effects, the pressure field contributes to material degradation [42, 43]. As shown in Figure 10, the static pressure at the Spool 31 emergency cover reaches 59.4 kPa.

The overlap between high velocity (9.04 m/s, Figure 8(d)) and elevated pressure results in combined tangential and normal stresses, explaining the severe material loss observed at the 90° position (10.7 mm).

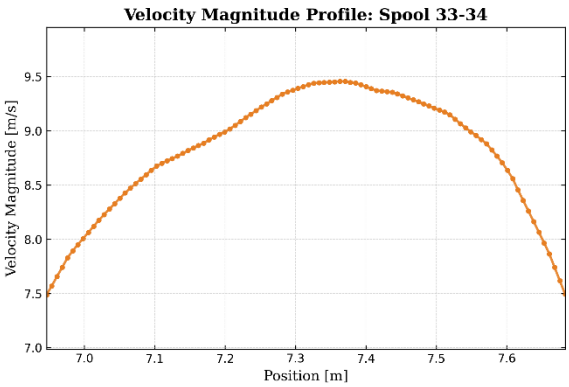

(a) Spool 33–34 velocity profile (curvature entry)

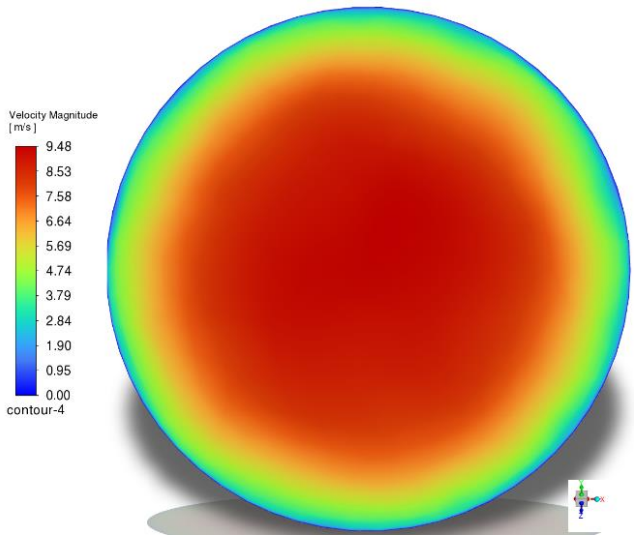

(b) Spool 33–34 cross-sectional contour

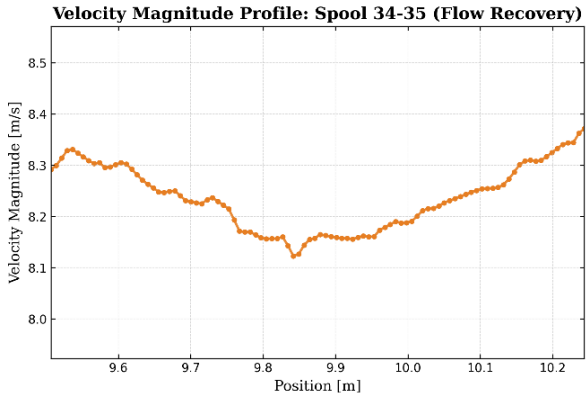

(c) Spool 34–35 velocity profile (flow recovery)

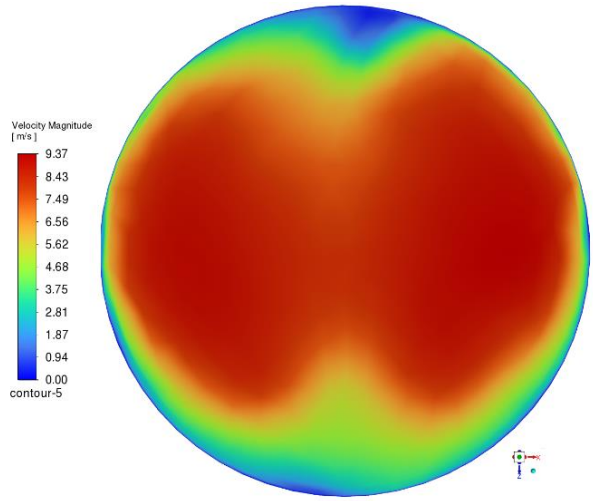

(d) Spool 34–35 cross-sectional contour

Figure 9. Velocity distribution across the verticalization elbow

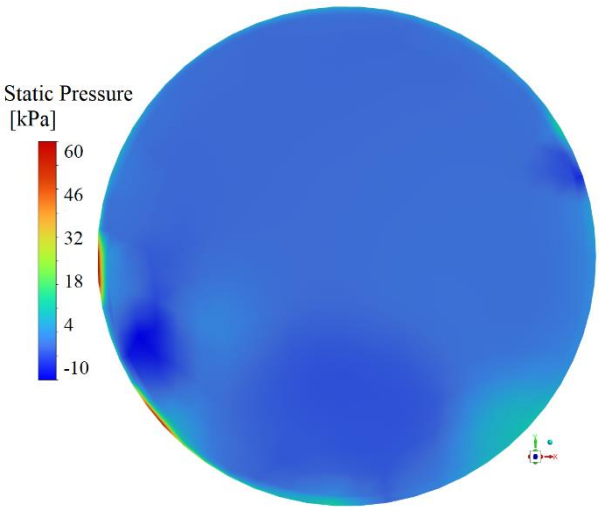

Figure 10. Static pressure distribution at the Spool 31 emergency cover transition

4.1.5 Particle trajectories and residence time analysis

To complete the hydrodynamic characterization, the discrete phase behavior was analyzed through Velocity Magnitude Pathlines and Particle Residence Time [44, 45]. While the carrier phase follows the pipeline geometry, coarse particles exhibit significant inertial deviation due to Stk $\gg$ 1 (Eq. (13)), particularly at the Y-junction transition. As shown in Figure 11, the pathlines near the Spool 31 emergency cover reveal a recirculating vortex structure [11, 12].

The velocity magnitude within these trajectories remains high, indicating that particles do not exit the junction in a streamlined manner but are instead subjected to rotational motion. This behavior increases impact frequency and produces a localized "sandblasting" effect, which is consistent with the wear patterns observed during field inspections.

The Particle Residence Time distribution (Figure 12) further identifies stagnation regions near the junction boundaries, where particles remain for extended periods, reaching values up to $4.08 \times 10^2\ s$ in critical zones [46, 47]. This prolonged exposure significantly amplifies cumulative erosion.

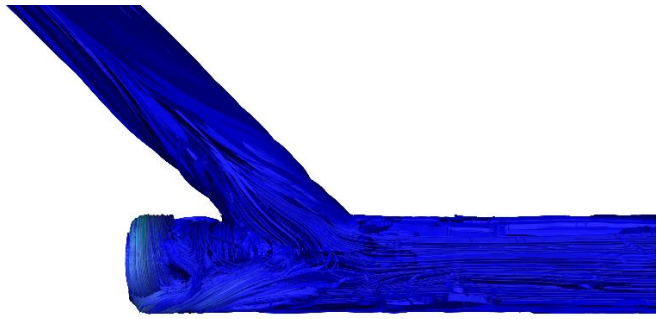

(a) Lateral view of the assembly

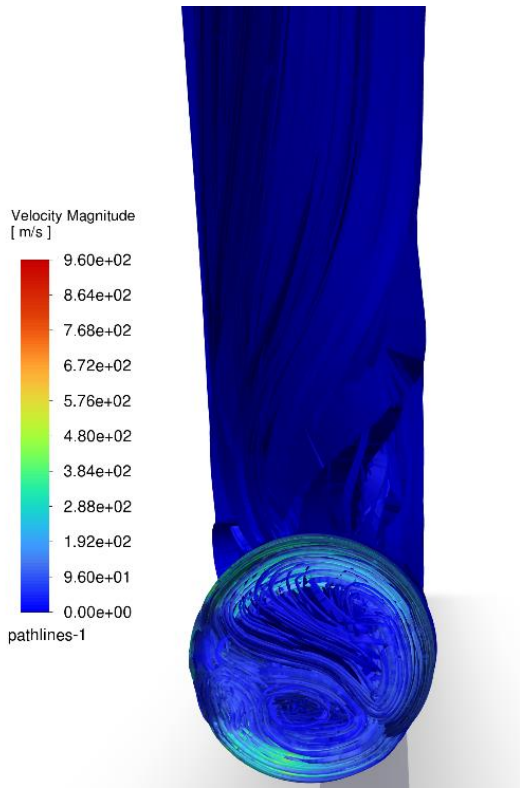

(b) Rear view focus on the Spool 31 emergency cover transition

Figure 11. Velocity magnitude pathlines for the solid phase

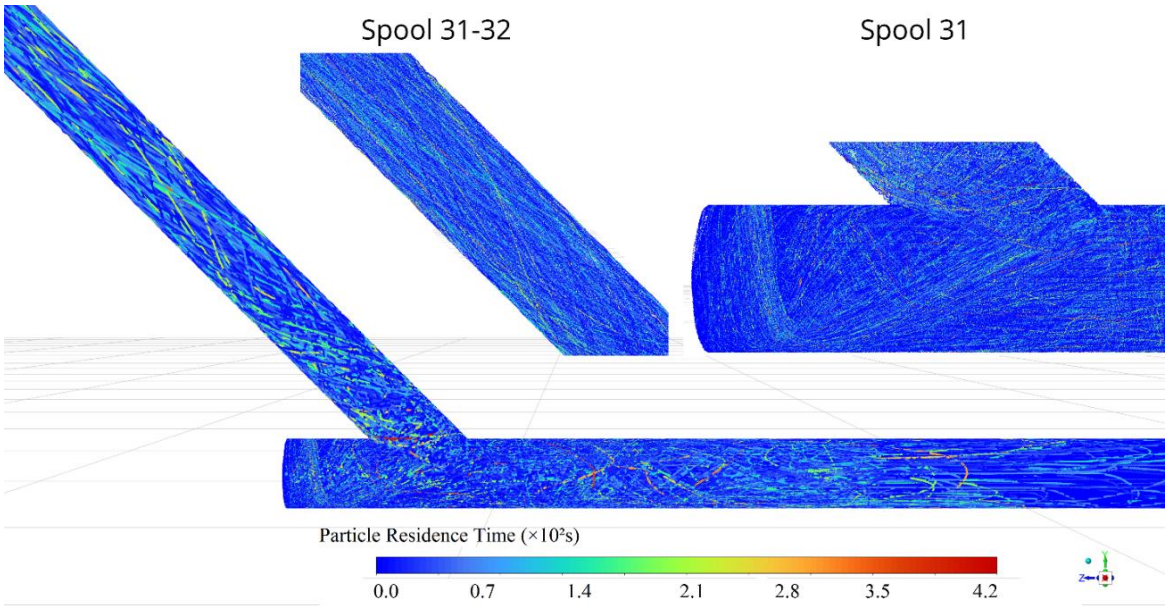

Figure 12. Particle Residence Time distribution. Lateral view of the spool assembly with detailed zooms of the Spool 31–32 junction and the Spool 31 emergency cover area

The convergence of high velocity (9.04 m/s, Figure 8(d)), elevated pressure (59.4 kPa, Figure 10), recirculating particle trajectories, and extended residence time (408 s) provides a consistent mechanistic explanation for the severe lining depletion observed at the 90° position (10.7 mm residual thickness).

4.2 Spatial erosion mapping: Hotspot identification and material strategy

The implementation of the Oka erosion model (Eqs. (14)–(18)) enabled the generation of a spatially resolved erosion map. As illustrated in Figure 13, a dominant hotspot is located at the bifurcation vertex of Spool 31, extending into the Spool 31–32 transition.

The DPM erosion rate isosurfaces indicate peak values of 3021 kg/(m²·s), while the general surface distribution is concentrated within the range of 9.00×10^{-7} to 1.00×10^{-6} kg/(m²·s).

This gradient confirms that erosion is highly localized rather than uniformly distributed along the liner surface.

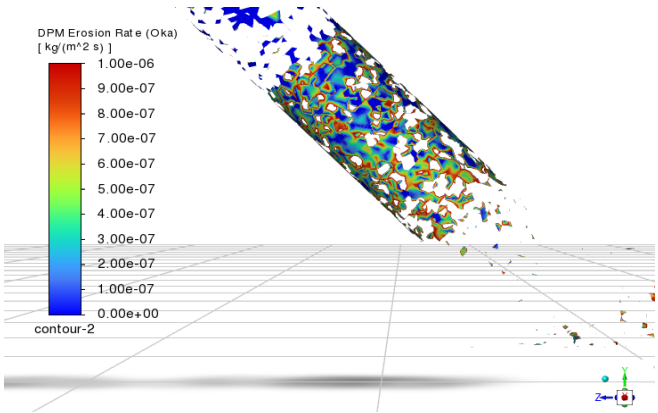

Figure 13. Discrete Phase Modeling (DPM) Erosion Rate isosurfaces at the Spool 31–32 junction

To quantify these results, the hydrodynamic and erosive parameters are summarized in Table 7, including Reynolds number, wall shear stress, peak erosion rate, and predicted service life for the critical components.

Table 7. Comparative analysis of hydrodynamic energy and erosive response across critical components

Component	local Reynolds Number (Re)	Wall Shear Stress (Pa)	Peak Erosion Rate (kg/(m²·s))	Predicted Service Life (Days)
Spool 31 (Y-Junction)	1.2×10^6	145.2	3021	112
Spool 34 (Elbow)	8.9×10^5	98.4	1850	185
Spool 38 (Outlet)	6.4×10^5	42.1	420	>365

4.2.1 Operational reliability and material upgrade recommendation

A key outcome of this analysis is the mismatch between material resistance and local hydrodynamic conditions at the Spool 31–32 transition. Spool 31 incorporates an alumina ceramic lining (Al_2O_3), whereas Spool 32 relies on an SBR rubber liner.

As shown in Figure 14, the ceramic material exhibits significantly lower volumetric loss due to its high hardness, while the rubber lining undergoes accelerated degradation. This is quantitatively supported by the predicted service life in Table 7, where Spool 31 reaches 112 days under extreme conditions, whereas Spool 32, subjected to similar hydrodynamic loads but lower material hardness, reaches the critical threshold of 10.7 mm residual thickness at approximately 112 to 120 days, consistent with UT measurements (Table 3).

Under continuous 24/7 operation, this service life is insufficient to reliably complete standard maintenance intervals. The hotspot identified in Figure 13, combined with the hydrodynamic conditions described in Section 4.1 (velocity up to 9.04 m/s and pressure up to 59.4 kPa), demonstrates that the local erosive environment exceeds the

mechanical resistance of the elastomeric lining.

Therefore, replacing the rubber lining in Spool 32 with an alumina-based ceramic system is not an empirical assumption but a physically justified design requirement. This upgrade is expected to align material resistance with the imposed hydrodynamic loads, ensuring operational continuity over a full maintenance cycle without critical depletion.

4.3 Mechanistic correlation: Field validation and Normalized Root Mean Square Error

To assess the predictive capability of the model, the simulated erosion depth was correlated with UT data obtained via the SIUI SMARTOR. It should be noted that UT measurements were conducted on Spool 32, as direct inspection of the ceramic-lined Spool 31 is limited by acoustic impedance constraints; therefore, the validation is performed indirectly through downstream thickness measurements.

The statistical fit was evaluated using the Normalized Root Mean Square Error (NRMSE), which provides a measure of the global deviation between numerical predictions and experimental measurements:

$$NRMSE = \frac{\sqrt{\frac{1}{n}\sum_{i=1}^{n}\left(y_{exp,i} - y_{sim,i}\right)^2}}{y_{max} - y_{min}} \qquad (19)$$

A parity diagram was constructed to compare the predicted and measured material thickness at 12 specific coordinates along the Spool 31–32 assembly, as shown in Figure 14.

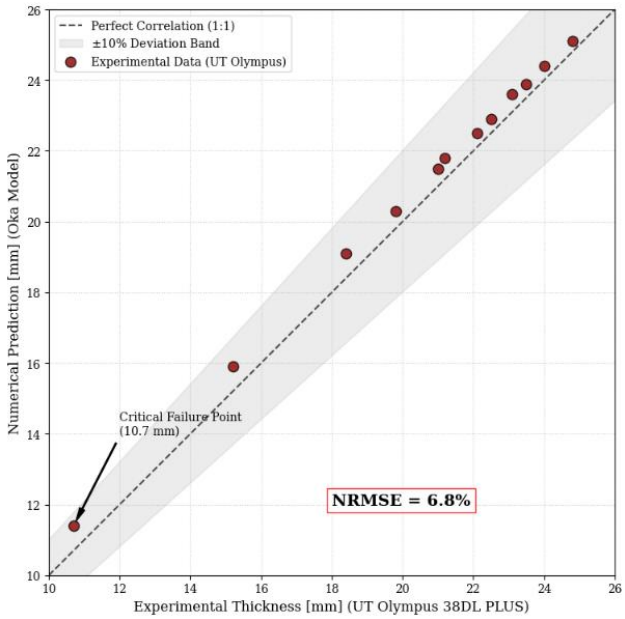

Figure 14. Parity plot of experimental vs. numerical thickness results

The comparative dataset used for this calculation, including local error analysis for both ceramic and rubber-lined regions, is detailed in Table 8. The resulting global error was 6.8% NRMSE, indicating good agreement between the Eulerian-Lagrangian framework and the observed material degradation. As observed in the parity plot (Figure 14), all validation points remain within the ±10% deviation band, with the model capturing the critical failure point of 10.7 mm in the rubber-lined section.

It is important to note that this level of agreement is subject to uncertainties associated with mesh discretization, rheological parameter variability (Table 5), and erosion model constants (Table 6), which may influence local predictions of peak wear.

This level of agreement suggests that the Herschel–Bulkley model (Eq. (9)) adequately represents the energy dissipation and non-Newtonian behavior of the slurry under the evaluated conditions. Consequently, the model was used to estimate the RUL of the component, as illustrated in Figure 15.

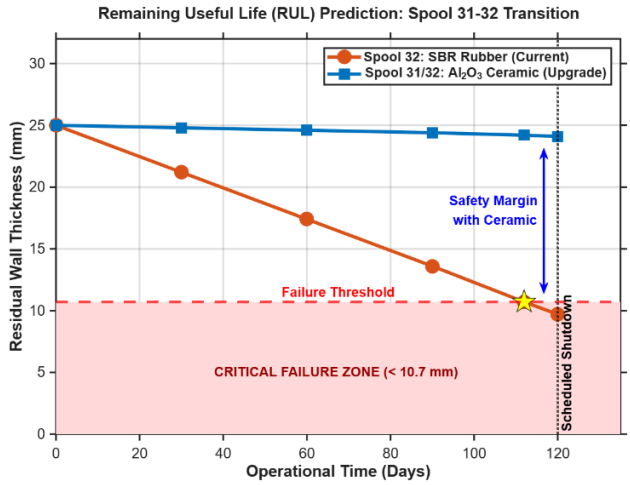

Figure 15. Comparative wear life and Remaining Useful Life (RUL) prediction

The prognostic analysis indicates that the current SBR rubber lining reaches the critical threshold at approximately 112 days, failing to complete the scheduled 120-day operational cycle, whereas the proposed alumina ceramic upgrade maintains structural integrity throughout the same period.

4.4 Material performance scaling and erosion regime justification

The material selection strategy is further reinforced by analyzing the scaling behavior of erosion as a function of material hardness and impact velocity. While Figure 15 provides a time-dependent prediction of liner degradation under operational conditions, it does not explicitly isolate the intrinsic material response governing erosion resistance.

To address this, an erosion regime map derived from Oka model scaling is presented in Figure 16, where the erosion rate is expressed as a function of impact velocity and Vickers hardness in logarithmic scale. This representation captures the strong non-linear dependence of erosion on both variables and allows direct comparison between material regimes.

At the characteristic operating condition of the system (impact velocity approximately 9 m/s), the elastomeric lining (SBR rubber, $H_v = 0.03$) is located within a high-erosion domain, whereas alumina ceramic ($H_v = 1550$) lies in a region where erosion rates are several orders of magnitude lower. This separation confirms that the difference in predicted service life observed in Figure 15 is primarily governed by intrinsic material properties rather than operational variability.

The combined interpretation of Figures 15 and 16 demonstrates that the premature failure of the rubber lining is not a consequence of localized anomalies but a direct result of its limited hardness under high-energy particle impacts.

Consequently, the transition to an alumina-based lining in Spool 32 is supported not only by numerical prediction and field validation, but also by the fundamental scaling behavior of erosion.

Table 8. Comparative dataset for model validation: Ultrasonic Testing (UT) Measurements vs. Computational Fluid Dynamics (CFD) Predictions

Control Point (CP)	Location Description	Liner Material	UT Measured (mm)	CFD Predicted (mm)	Local Relative Error (%)
CP-01	Spool 31 - Inlet Zone	Ceramic (Al_2O_3)	25.0	25.2	0.8%
CP-02	Spool 31 - Lateral Wall	Ceramic (Al_2O_3)	23.8	24.1	1.3%
CP-03	**Spool 31 - Junction Vertex**	**Ceramic (Al_2O_3)**	**21.2**	**21.8**	**2.8%**
CP-04	Spool 31 - Access Door	Ceramic (Al_2O_3)	22.5	22.9	1.8%
CP-05	Spool 32 - Interface Start	Rubber (SBR)	18.4	19.2	4.3%
CP-06	**Spool 32 - Critical Hotspot**	**Rubber (SBR)**	**10.7**	**11.4**	**6.5%**
CP-07	Spool 32 - Impact Zone	Rubber (SBR)	12.1	12.9	6.6%
CP-08	Spool 32 - Body (Upper)	Rubber (SBR)	14.5	15.3	5.5%
CP-09	Spool 32 - Body (Lower)	Rubber (SBR)	16.2	16.8	3.7%
CP-10	Spool 32 - Exit Flange	Rubber (SBR)	19.8	20.4	3.0%
CP-11	Radial Reference A	Mixed	22.1	22.5	1.8%
CP-12	Radial Reference B	Mixed	23.4	23.8	1.7%
Average	**Global System**	--	**19.1**	**19.7**	**3.1%**

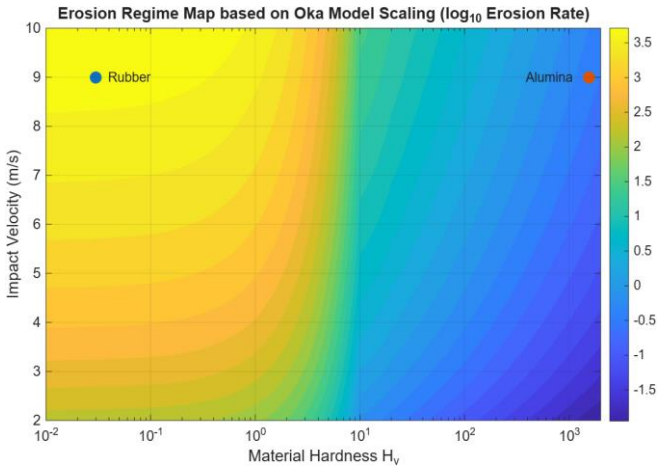

Figure 16. Erosion regime map based on Oka scaling

The combined interpretation of Figures 15 and 16 demonstrates that the premature failure of the rubber lining is not a consequence of localized anomalies but an inherent limitation of its mechanical resistance under high-energy particle impacts. Consequently, the transition to an alumina-based lining in Spool 32 is supported not only by numerical prediction and field validation, but also by the fundamental scaling behavior of erosion.

5. CONCLUSIONS

The transition from empirical maintenance to data-driven reliability in the grinding classification circuit demonstrates that the implemented Eulerian Lagrangian framework provides a consistent physical representation of hydro-abrasive wear mechanisms under industrial operating conditions. The model, supported by an NRMSE of 6.8%, confirms that the initial material distribution, prioritizing alumina ceramic (Al_2O_3) in primary impact zones such as the Y-junction (Spool 31) and the high-curvature elbow (Spool 34), is appropriate for regions subjected to direct particle impingement. At the same time, the results reveal that asymmetric flow redistribution extends erosive loads beyond these zones, exposing downstream components to critical conditions not captured by conventional design assumptions.

Within this framework, Spool 32 is identified as a critical vulnerability, where local hydrodynamic conditions generate particle impact energies that exceed the mechanical resistance of the SBR rubber lining. The predicted minimum thickness of 10.7 mm, consistent with field measurements, demonstrates that the observed failure is governed by localized momentum concentration rather than uniform material degradation. This agreement, although based on indirect ultrasonic measurements, provides a consistent validation baseline for assessing model predictability under real operating conditions.

The integration of numerical prediction, field measurements, and erosion scaling analysis establishes a coherent interpretation of material performance. In particular, the erosion regime map (Figure 16) shows that elastomeric and ceramic linings operate in fundamentally different erosion domains, governed primarily by material hardness under equivalent impact velocities. This scaling behavior explains the degradation trends observed in Figure 15 and provides a mechanistic basis for material selection beyond empirical observation.

Although the present study is based on a single industrial configuration, the combined framework, linking hydrodynamics, particle tracking, erosion kinetics, and material scaling, offers a transferable methodology for evaluating wear in slurry transport systems with similar operating regimes. Within this context, the premature failure of the rubber lining is identified as an inherent material limitation rather than an isolated operational anomaly. Consequently, replacing the Spool 32 lining with an alumina-based ceramic system constitutes a physically justified design decision, enabling improved reliability across the maintenance cycle and reducing the likelihood of unplanned operational interruptions.

ACKNOWLEDGMENT

We thank the Universidad Nacional de San Agustín de Arequipa for their support and knowledge.

REFERENCES

[1] Both, C., Dimitrakopoulos, R. (2021). Applied machine

learning for geometallurgical throughput prediction-A case study using production data at the tropicana gold mining complex. Minerals, 11(11): 1257. https://doi.org/10.3390/min11111257

[2] Reichl, C., Schatz, M., Zsak, G. (2016). World Mining Data-Minerals Production. Vienna: International Organizing Committee for the World Mining Congresses. https://data.opendevelopmentcambodia.net/dataset/66410c8b-083d-4225-abe8-3e56b69e3984/resource/c25f7837-9ac0-4b16-955d-bcc6da452bd5/download/wmd2017.pdf.

[3] Gahlot, V.K., Seshadri, V., Malhotra, R.C. (1992). Effect of density, size distribution, and concentration of solid on the characteristics of centrifugal pumps. Journal of Fluids Engineering, 114(3): 386-389. https://doi.org/10.1115/1.2910042

[4] Jeswiet, J., Szekeres, A. (2016). Energy consumption in mining comminution. Procedia CIRP, 48: 140-145. https://doi.org/10.1016/j.procir.2016.03.250

[5] Ghasemi, Z., Neumann, F., Zanin, M., Karageorgos, J., Chen, L. (2023). A comparative study of prediction methods for semi-autogenous grinding mill throughput. Minerals Engineering, 205: 108458. https://doi.org/10.1016/j.mineng.2023.108458

[6] Varghese, A., Martins, S., Lessing, E., Hassan, G., Karrech, A. (2025). A systematic review on the sustainability of slurry pumps in the mining industry. Minerals Engineering, 234: 109731. https://doi.org/10.1016/j.mineng.2025.109731.

[7] Varghese, A., Martins, S., Lessing, E., Hassan, G.M., Karrech, A. (2022). Pumping sustainably-power and water consumption in mineral processing plants: Someone should care. In: IMPC Asia Pacific 2022 Conference Proceedings, pp. 1506-1527. https://research-repository.uwa.edu.au/en/publications/pumping-sustainably-power-and-water-consumption-in-mineral-proces/.

[8] Sun, C., Xiao, Z., Xiao, Y., Xu, Z., Cui, W., Wang, P., Fang, Z., Cui, G., Jia, L. (2024). Research on multi-objective optimization method of Z-shaped pipeline structure based on Kriging model. Scientific Reports, 14(1): 1-19. https://doi.org/10.1038/s41598-024-81130-6

[9] Sellgren, A., Visintainer, R., Furlan, J., Matoušek, V. (2016). Pump and pipeline performance when pumping slurries with different particle gradings. The Canadian Journal of Chemical Engineering, 94(6): 1025-1031. https://doi.org/10.1002/cjce.22489

[10] Ji, Y., Tong, J., Zhang, Y., Xu, X., Zhao, Y., Zhu, J. (2024). Numerical prediction of the effect of typical particle properties on a centrifugal pump. IEEE Access, 12: 79905-79918. https://doi.org/10.1109/access.2024.3409454

[11] Moll, R., Moulin, P., Veyret, D., Charbit, F. (2002). Numerical simulation of Dean vortices: Fluid trajectories. Journal of Membrane Science, 197(1-2): 157-172. https://doi.org/10.1016/s0376-7388(01)00606-8

[12] Saffar, Y., Kashanj, S., Nobes, D.S., Sabbagh, R. (2023). The physics and manipulation of dean vortices in single- and two-phase flow in curved microchannels: A review. Micromachines, 14(12): 2202. https://doi.org/10.3390/mi14122202

[13] Sangal, S., Singhal, M.K., Saini, R.P. (2018). Hydro-abrasive erosion in hydro turbines: A review. International Journal of Green Energy, 15(4): 232-253. https://doi.org/10.1080/15435075.2018.1431546

[14] Singh, H. (2026). Challenges of Corrosion, Wear, Erosion, and Abrasion in Hydropower Plants: Materials, Modeling, and Mitigation Strategies. Engineering Transactions. https://doi.org/10.24423/engtrans.2026.3574

[15] Kumar, S., Khanna, V. (2024). Thermal Spray Coatings: Materials, Techniques & Applications. pp. 76-95. Bentham Science Publishers. https://doi.org/10.2174/9789815223552124010l

[16] Singh, J., Kumar, S., Gill, H.S. (2023). Review on testing facilities assisting in development of numerical models for erosion calculation in centrifugal slurry pumps. International Journal on Interactive Design and Manufacturing (IJIDeM), 18(8): 5301-5327. https://doi.org/10.1007/s12008-023-01282-z

[17] Borkowski, P.J. (2020). Comminution of copper ores with the use of a high-pressure water jet. Energies, 13(23): 6274. https://doi.org/10.3390/en13236274

[18] Zhironkina, O., Zhironkin, S. (2023). Technological and intellectual transition to mining 4.0: A review. Energies, 16(3): 1427. https://doi.org/10.3390/en16031427

[19] Fragassa, C., Pavlovic, A., Arru, M., et al. (2026). Thermo-mechanical response of an automotive power module heat sink under combined thermal and power cycling. Journal of Complex and Multiphysics Engineering Systems, 1(2): 122-137. https://doi.org/10.56578/jcmes010201

[20] Ton-That, H.L. (2026). Identification of damage in planar truss structures within a multiphysics framework using metaheuristic optimization algorithms. Journal of Complex and Multiphysics Engineering Systems, 1(2): 138-147. https://doi.org/10.56578/jcmes010202

[21] Pan, H., Xie, S., Gu, W., Song, T., Qiu, F., Chen, D. (2025). Research on key parameters and engineering experiments of coal gangue slurry filling technology. Applied Sciences, 15(10): 5475. https://doi.org/10.3390/app15105475

[22] Lopez, P., Reyes, I., Risso, N., Momayez, M., Zhang, J. (2023). Machine learning algorithms for semi-autogenous grinding mill operational regions' identification. Minerals, 13(11): 1360. https://doi.org/10.3390/min13111360

[23] Yang, X., Xi, T., Qin, Y., Zhang, H., Wang, Y. (2024). Computational Fluid Dynamics-discrete phase method simulations in process engineering: A review of recent progress. Applied Sciences, 14(9): 3856. https://doi.org/10.3390/app14093856

[24] Chang, P., Xu, G., Zhou, F., Mullins, B., Abishek, S. (2019). Comparison of underground mine DPM simulation using discrete phase and continuous phase models. Process Safety and Environmental Protection, 127: 45-55. https://doi.org/10.1016/j.psep.2019.04.027

[25] Visintainer, R., Matoušek, V., Pullum, L., Sellgren, A. (2023). Slurry Transport Using Centrifugal Pumps. Springer Nature. https://doi.org/10.1007/978-3-031-25440-6

[26] Wang, S., Yu, H., Wu, R., Tang, M., Liu, Y., Liu, L., Song, X. (2024). Study on ultra-long-distance transportable concentration gradient of coal gangue

slurry with different gradations. Minerals, 14(5): 487. https://doi.org/10.3390/min14050487
[27] Gu, W., Yang, B., Pan, H., Song, T. (2023). Research and engineering practice on space characteristics of gangue slurry filling. Scientific Reports, 13(1): 1-15. https://doi.org/10.1038/s41598-023-46222-9
[28] Wang, Y., Tang, X., Ju, F., Xiao, M., Wang, T., Wang, D., Yin, L., Si, L., Xu, M. (2025). Experimental optimization study on pumping pipeline transportation performance of pure gangue slurry filling material. Materials, 18(20): 4788. https://doi.org/10.3390/ma18204788
[29] Wang, Y., Li, H., Huang, G., Liang, Q., Cheng, Q. (2024). Rheological properties of gangue-filled slurry based on L-pipe experiments. Canadian Metallurgical Quarterly, 64(3): 1437-1448. https://doi.org/10.1080/00084433.2024.2395638
[30] Blazek, J. (2015). Computational Fluid Dynamics: Principles and Applications. Butterworth-Heinemann.
[31] Thakur, L., Vasudev, H. (2021). Thermal Spray Coatings. Taylor & Francis. https://doi.org/10.1201/9781003213185
[32] Wei, J., Liu, L., Wang, S., Wei, B., Qin, X., Liu, Z., Huang, C., Jia, Q., Zhuang, D., Huang, X. (2025). Dynamic characteristics of gangue slurry flow in pipelines under blockage conditions: Numerical Simulations. Powder Technology, 468. https://doi.org/10.1016/j.powtec.2025.121675
[33] Reddy, N.V.K., Pothal, J.K., Barik, R., Senapati, P.K. (2023). Pipeline slurry transportation system: An overview. Journal of Pipeline Systems Engineering and Practice, 14(3): 1391. https://doi.org/10.1061/jpsea2.pseng-1391
[34] Zhang, J., He, X., Yang, K., Wei, Z., Zhao, X., Fang, J. (2023). Diffusion law of coal gangue slurry and the application of fluidized filling technology of gangue in caving area. Scientific Reports, 13(1): 1-13. https://doi.org/10.1038/s41598-023-38165-y
[35] Chhabra, R.P., Patel, S.A. (2025). Non-Newtonian flow and applied rheology: Engineering applications. Elsevier.
[36] Kolev, N.I. (2015). Numerical solution methods for multi-phase flow problems. In Multiphase Flow Dynamics 1: Fundamentals, pp. 497-602. https://doi.org/10.1007/978-3-642-20605-4_12
[37] Hutchings, I., Shipway, P. (2017). Tribology: Friction and Wear of Engineering Materials. Butterworth-Heinemann.
[38] Zhu, L., Li, Z., Wu, Y., Liu, C., Zhang, D., Chai, J., Gu, W., Ding, Z., Gao, L., Qiu, F., Ma, C. (2025). CFD numerical simulation of slurry flow characteristics under the clogged form of coal gangue slurry transportation pipeline. Applied Sciences, 15(4): 1957. https://doi.org/10.3390/app15041957
[39] El-Emam, M.A., Zhou, L., Yasser, E., Bai, L., Shi, W. (2022). Computational methods of erosion wear in centrifugal pump: A state-of-the-art review. Archives of Computational Methods in Engineering, 29(6): 3789-3814. https://doi.org/10.1007/s11831-022-09714-x
[40] Liu, J., Pang, J., Liu, X., Huang, Y., Deng, H. (2023). Analysis of sediment and water flow and erosion characteristics of large Pelton turbine injector. Processes, 11(4): 1011. https://doi.org/10.3390/pr11041011
[41] Singh, J., Kumar, S. (2025). Slurry Erosion. Taylor & Francis. https://doi.org/10.1201/9781003561156
[42] Yang, J., Yang, B., Yu, M. (2019). Pressure study on pipe transportation associated with cemented coal gangue fly-ash backfill slurry. Applied Sciences, 9(3): 512. https://doi.org/10.3390/app9030512
[43] Wu, D., Yang, B., Liu, Y. (2015). Pressure drop in loop pipe flow of fresh cemented coal gangue – fly ash slurry: Experiment and simulation. Advanced Powder Technology, 26(3): 920-927. https://doi.org/10.1016/j.apt.2015.03.009
[44] Shi, Z., Zhao, H., Liang, B., Sun, W., Wang, J., Fang, S. (2023). Simulation test study on filling flow law of gangue slurry in goaf. Scientific Reports, 13(1): 1-16. https://doi.org/10.1038/s41598-023-45596-0
[45] Gu, W., Wang, Y., Xu, D., Miao, K., Yao, S., Zhang, H., Han, Z. (2024). Numerical study of gangue slurry deposition behavior in pipelines considering viscosity change. Minerals, 14(3): 318. https://doi.org/10.3390/min14030318
[46] Zhen, Y., Li, W., Ren, Y.Q., Zhang, Y.H., Chen, X., Zhang, H. (2026). Pipeline transportation characteristics of pure coal gangue filling slurry. Engineering Research Express, 8(1): 015111. https://doi.org/10.1088/2631-8695/ae310b
[47] Liu, B., Zhang, Y., Yang, S. (2025). Influence of coal gangue-aeolian sand aggregate gradation on rheological properties and pipeline transportation characteristics of filling slurry. Scientific Reports, 15(1): 1-12. https://doi.org/10.1038/s41598-024-84955-3

NOMENCLATURE

A_{face}	face area of the computational cell, m^2
Ar	Archimedes number, dimensionless
C_D	Drag coefficient, dimensionless
d_p	Particle diameter, m
E_{90}	Erosion rate at normal impact (90°), $kg \cdot m^{-2} \cdot s^{-1}$
$E(\alpha)$	erosion rate as a function of impact angle, $kg \cdot m^{-2} \cdot s^{-1}$
$\dot{E}_{mass}$	mass erosion rate, $\frac{kg}{s}$
E_v	volumetric erosion rate, $m^3 \cdot s^{-1}$
e_n	normal restitution coefficient, dimensionless
e_t	tangential restitution coefficient, dimensionless
F	external body forces vector, N/m^3
F_D	drag force per unit particle mass, s^{-1}
F_L	Saffman lift force vector, N/kg
F_{other}	additional force vectors, N/kg
F_s	safety factor for GCI analysis, dimensionless
g	gravitational acceleration vector, $\frac{m}{s^2}$
GCI	Grid Convergence Index, dimensionless
H	hydraulic head, m
H_v	Vickers hardness of the material, Pa
$k1$, $k2$, $k3$	empirical constants for Oka model, dimensionless
L	characteristic length, m
N	number of data points, dimensionless
n	flow behavior index, dimensionless
$n1$, $n2$	Oka impact angle exponents, dimensionless

$NRMSE$	Normalized Root Mean Square Error, dimensionless
P	power, W
p	static pressure, Pa
Q	volumetric flow rate, m^3/s^{-1}
R^2	coefficient of determination, dimensionless
$R_{erosion}$	linear erosion rate, $\frac{m}{s}$
Re	Reynolds number, dimensionless
r	grid refinement ratio, dimensionless
Stk	Stokes number, dimensionless
t	time, s
$\boldsymbol{u}$	fluid velocity vector, $\frac{m}{s}$
$\boldsymbol{u}_p$	particle velocity vector, $\frac{m}{s}$
u_τ	friction velocity, $\frac{m}{s}$
$u - u_p$	relative velocity (fluid–particle), $m \cdot s^{-1}$
$\boldsymbol{v}$	velocity vector, $\frac{m}{s}$
v_p	particle impact velocity, $\frac{m}{s}$
y	distance to the wall, m
y^+	dimensionless wall distance, dimensionless
$\overline{y}$	mean observed value, dimensionless
y_{exp}	experimental value, dimensionless
y_{sim}	simulated value, dimensionless
$\hat{y}_i$	predicted value, dimensionless
τ_p	particle relaxation time, s

Greek symbols

α	impact angle, rad
$\dot{\gamma}$	shear rate, s^{-1}
ϵ	relative error for GCI, dimensionless
μ	dynamic viscosity, $kg \cdot m^{-1} \cdot s^{-1}$
ρ	fluid density, $\frac{kg}{m^3}$
ρ_p	particle density, $\frac{kg}{m^3}$
ρ_{wall}	wall material density, $\frac{kg}{m^3}$
τ	shear stress (Herschel–Bulkley model), Pa
$\overline{\tau}$	viscous stress tensor, Pa
τ_y	yield stress, Pa
∇	nabla operator, m^{-1}

Subscripts

1, 2	initial and final states
i	data point index
max, min	maximum and minimum values
p	particle phase